arXiv:2212.02489v1 [physics.chem-ph] 5 Dec 2022

Effect of Nano-Confinement on NMR Relaxation of Heptane in Kerogen from MD Simulations and Measurements†

Arjun Valiya Parambathu,‡,¶ Walter G. Chapman,‡ George J. Hirasaki,‡ Dilip Asthagiri,*,§ and Philip M. Singer*,‡

‡*Department of Chemical and Biomolecular Engineering, Rice University, 6100 Main St., Houston, TX 77005, USA*

¶*Department of Chemical and Biomolecular Engineering, 150 Academy St, University of Delaware, Newark, DE 19716, USA*

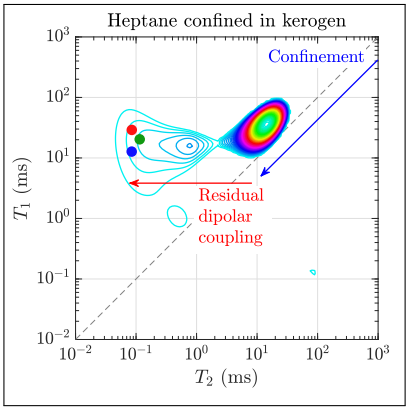
§*Oak Ridge National Laboratory, 1 Bethel Valley Road, Oak Ridge, TN 37830-6012*

E-mail: asthagiridn@ornl.gov; ps41@rice.edu

Abstract

Kerogen-rich shale reservoirs will play a key role during the energy transition, yet the effects of nano-confinement on the NMR relaxation of hydrocarbons in kerogen are poorly understood. We use atomistic MD simulations to investigate the effects of nano-confinement on the ^{1}H NMR relaxation times T_1 and T_2 of heptane in kerogen. In the case of T_1, we discover the important role of confinement in reducing T_1 by ∼3 orders of magnitude from bulk heptane, in agreement with measurements of heptane dissolved in kerogen from the Kimmeridge Shale, *without any models or free parameters*. In the case of T_2, we discover that confinement breaks spatial isotropy and gives rise to residual dipolar coupling which reduces T_2 by ∼5 orders of magnitude from bulk heptane. We use the simulated T_2 to calibrate the surface relaxivity and thence predict the pore-size distribution of the organic nano-pores in kerogen, *without additional experimental data.*

Graphical TOC Entry



†Notice: This manuscript has been authored by UT-Battelle, LLC, under contract DE-AC05-00OR22725 with the US Department of Energy (DOE). The US government retains and the publisher, by accepting the article for publication, acknowledges that the US government retains a nonexclusive, paid-up, irrevocable, worldwide license to publish or reproduce the published form of this manuscript, or allow others to do so, for US government purposes. DOE will provide public access to these results of federally sponsored research in accordance with the DOE Public Access Plan (http://energy.gov/downloads/doe-public-access-plan).

Kerogen is a high molecular-weight organic matter that serves as source and reservoir for all hydrocarbons in "shale". Kerogen-rich shale reservoirs will most certainly play a key role during the energy transition, with it providing a clean burning energy source, as well as a sink for carbon capture and storage. This strategy requires us to have an accurate mapping of the subterranean shale formation, since the "sweet spots" for economical extraction via fracking[1] and CO_2 sequestration[2] are an intimate function of the local structure of the extremely heterogeneous shale formations. Among the many tools used in characterizing the reservoirs, NMR (nuclear magnetic resonance) logging is at the forefront.

The interpretation of NMR logs still relies on traditional theories[3,4] that make rather strong assumptions regarding molecular structure and interactions. For example, the seminal Bloembergen, Purcell, Pound (BPP) theory for *intra*molecular ^{1}H-^{1}H dipole-dipole relaxation assumes molecules are hard spheres that undergo free rotation. This model is the basis for modeling NMR relaxation in liquids and predicts that T_1 increases with viscosity ($T_1 \propto \eta/T$) at high viscosity. However, for highly viscous or nanoconfined liquids, i.e. in the slow-motion region, experimental results[5–12] show that T_1 becomes independent of η/T. The literature commonly attributes this deviation by invoking the physics of paramagnetism,[13] or it is attributed to the presence of organic nano-pores in the system that confines the small molecules and enhances their ^{1}H-^{1}H dipole-dipole relaxation.[12]

In a series of papers since 2017,[11,12,15–19] we have used atomistic MD (molecular dynamics) simulations to clarify the fundamental physics underlying NMR relaxation in fluids entirely avoiding the assumptions in traditional theories and without using *adjustable* parameters. We found that *intra*molecular ^{1}H-^{1}H dipole-dipole relaxation in the fast-motion (i.e., low viscosity) regime for bulk water and alkanes[15,16,18] is not a mono-exponential as predicted by BPP while predicting $T_{1,2}$ in agreement with measurements. The simulations have helped clarify the importance of molecular flexibility[16] and spin-rotation[17] in the relaxation response and revealed the ability of simulations to capture relaxation in the presence of the paramagnetic Gd^{3+}.[20,21] In particular, for n-heptane in a viscous polymer matrix,[11,12,19] simulations showed that the anomalous T_1 plateau at high viscosity emerges due to nano-confinement, and a feature that had been explained by invoking paramagnetism.[13]

Here we study the ^{1}H-^{1}H dipole-dipole relaxation of heptane in realistic kerogen models. Modeling kerogen is an arduous task and researchers have taken quite different approaches. We focus on two models: CS1000a, a rigid carbon matrix that has a pore distribution similar to Marcellus kerogen,[22,23] and kerogen-IIC, a flexible molecular model of kerogen that respects the chemical composition based on an oil-prone mature kerogen from marine shales.[24,25] We also include our previous results of heptane-polymer mixes,[19] where the viscous polymer acts as a model for immature kerogen. All simulations presented here are at 25°C, and all measurements are at 30°C.

Table 1: Summary of simulation results for confined heptane.

Confining matrix	ϕ_μ (vol%)	$\mathcal{T}$ (–)	$\langle\tau\rangle$ (ps)	T_1 (ms)	$T_{2,RDC}$ (ms)
Bulk	100	1	1.8	8600	∞
CS1000a	58	80	870	29	0.085
Polymer 5:95	5	320	1500	20	0.120
Kerogen-IIC	15	370	1900	13	0.085

[a] Table includes percent volume of heptane ϕ_μ in the matrix, tortuosity of the matrix $\mathcal{T} = D_{bulk}/D_{sim}$ derived from the diffusion coefficient under confinement D_{sim} and bulk D_{bulk}, average correlation times $\langle\tau\rangle$ computed using Eq. 4, T_1 at $f_0 = 2.3$ MHz using Eq. 6, and residual dipolar coupling $T_{2,RDC}$ using Eq. 8. All quantities are derived without any models or free parameters.

The three different confining matrices are illustrated in Figure 1. Listed in Table 1 are the volume percent of heptane in the matrix, traditionally called "micro" porosity ϕ_μ.[26] The heptane in CS1000a is assumed to be fully saturated, and hence the porosity $\phi_\mu = 58$ vol% is the net free volume available in the CS1000a matrix.[22] For CS1000a, we also assume each

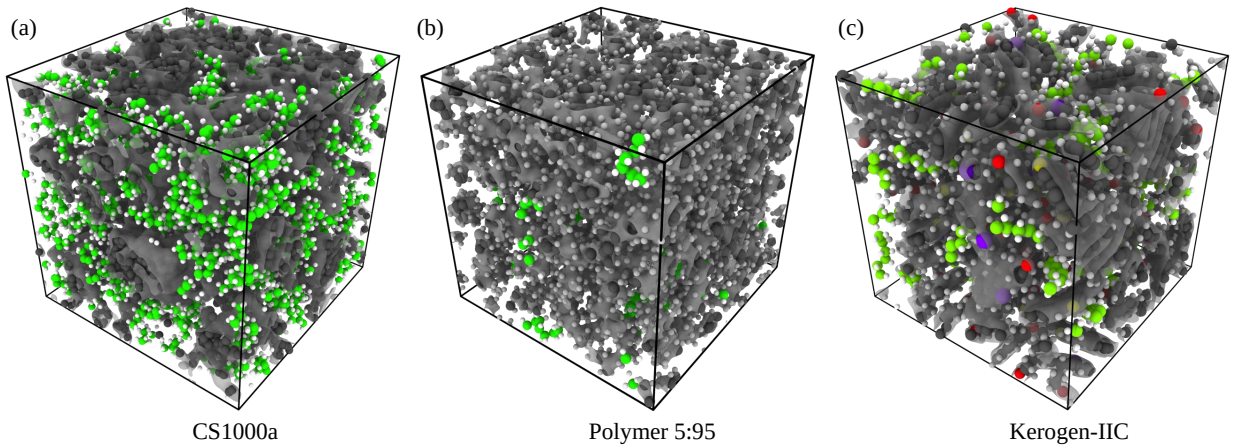


Figure 1: Equilibrated simulation boxes of heptane confined in (a) CS1000a (b) polymer at 5:95 volume ratio (c) kerogen-IIC. Heptane is in green (C) and white (H). The matrix is in black (C), gray (H), red (O), purple (S) and yellow (N), with a surface mesh. The images are generated using OVITO.[14]

matrix carbon atom as a site for ^{1}H dipole relaxation. The heptane-polymer mixture is prepared with 5:95 volume ratio, hence $\phi_\mu = 5$ vol%.[19] The heptane porosity in kerogen-IIC $\phi_\mu = 15.2$ vol% is adjusted based on swelling ratio, and is consistent with the measured porosity $\phi_\mu = 13.6$ vol% of dissolved heptane in Kimmeridge kerogen.[26] See SI for more details about the simulation.

T_1 **dispersion**: The ^{1}H-^{1}H dipole-dipole T_1 relaxation dispersion is derived from simulations by computing the autocorrelation function $G(t)$ for fluctuating magnetic ^{1}H-^{1}H dipole-dipole interactions in the system.[3,4,27–29] For an *isotropic* system, $G(t)$ is given as:

$$G(t) = \frac{1}{4}\left(\frac{\mu_0}{4\pi}\right)^2 \hbar^2\gamma^4 I(I+1)\times \frac{1}{N}\sum_{i\neq j}^{N}\left\langle \frac{(3\cos^2\theta_{ij}(t+t')-1)}{r_{ij}^3(t+t')}\frac{(3\cos^2\theta_{ij}(t')-1)}{r_{ij}^3(t')}\right\rangle_{t'} \quad (1)$$

where t is the lag time of the autocorrelation, μ_0 is the vacuum permeability, $\hbar$ is the reduced Planck constant, $\gamma/2\pi(= 42.58$ MHz/T) is the nuclear gyro-magnetic ratio for ^{1}H (spin $I = 1/2$), r_{ij} is the magnitude of the vector connecting the (i,j) ^{1}H-^{1}H dipole-pairs, θ_{ij} is the polar angle between $\vec{r}_{ij}$ and the external magnetic field $\vec{B}_0$, and N is the number of ^{1}H's associated with heptane in the simulation box. The autocorrelation function $G(t)$ can be computed using the positions of all the hydrogens from the simulation trajectory.

Note that we neglect the other harmonic terms for $G(t)$[29] in Eq. 1 since the system is "isotropic" over the length scale of the simulation box. Specifically, the orientation of an adsorbed heptane in kerogen is random with respect to $\vec{B}_0$, therefore the ensemble average over all randomly oriented heptane molecules averages out any preferred orientation over the length scale of the simulation box. This was confirmed by changing the direction of $\vec{B}_0$ in the simulation, resulting in a $\pm 6\%$ variation in T_1, which is consistent with uncertainties reported in Ref. 21. We note however that this would not generally be the case if the simulation were comprised of heptanes adsorbed onto a single nano-cylinder, for example; in such cases, all harmonic terms in $G(t)$ would be required, or a "powder average" is required.[30]

Once we have the autocorrelation function $G(t)$, we need the spectral density function $J(\omega)$ to compute T_1:

$$J(\omega) = 2\int_0^\infty G(t)\cos(\omega t)\,dt, \quad (2)$$

for $G(t)$ in units of $1/\text{s}^2$.[28] As we can see in Eq. 2, we ideally need the *entire* $G(t)$ curve to

compute T_1 dispersion. However, in the slow-motion regime, $G(t)$ does not completely decay to zero in simulation time scales. (We use a maximum lag time of $t_{max} = 3$ ns in $G(t)$ for trajectory data of length 10 ns.) We circumvent the role of limited data at large t by expanding $G(t)$ as

$$G(t) = \int_0^\infty P(\tau) \exp\left(-\frac{t}{\tau}\right) d\tau. \qquad (3)$$

and determining the underlying probability distribution $P(\tau)$ in correlation times τ,[12,19] where we interpret the peaks in $P(\tau)$ as dynamic molecular modes.[18] This inversion technique has also found recent success in high-T_c superconductors[31] and quantum spin liquids.[32] Notice that Eq. 3 is a Fredholm integral of the first kind with the kernal function $\exp(-t/\tau)$. We solve this using Tikhonov regularization to obtain $P(\tau)$, from which the average correlation time is defined as:

$$\langle\tau\rangle = \frac{1}{G(0)} \int_0^\infty P(\tau)\tau d\tau, \qquad (4)$$

Once we have the distribution $P(\tau)$, Eq. 2 reduces to the following:

$$J(\omega) = 2 \int_0^\infty \frac{\tau}{1 + (\omega\tau)^2} P(\tau) d\tau. \qquad (5)$$

and T_1 is given by:[28,29]

$$\frac{1}{T_1} = J(\omega_0) + 4J(2\omega_0), \qquad (6)$$

where $\omega_0 = 2\pi f_0 = \gamma B_0$ is the Larmor (i.e., resonance) frequency, and B_0 the applied magnetic field strength. In the fast-motion (i.e., low viscosity) regime defined as $\omega_0\langle\tau\rangle \ll 1$, $T_1 = T_2 \propto 1/\langle\tau\rangle$ and there is *no* dispersion in T_1. In the slow-motion (i.e., high viscosity) regime defined as $\omega_0\langle\tau\rangle \gg 1$, $T_1 > T_2$ and there *is* dispersion in T_1. For crude oils and polymers, the transition $\omega_0\langle\tau\rangle \simeq 1$ occurs at a viscosity of $\eta \simeq 6.4 \times 10^3\,\mathrm{cP}/f_0$ (at 25°C) for f_0 in (MHz) units.[33] A similar concept exists for fluids under nano-confinement, where $\langle\tau\rangle$ increases with the degree of confinement. See SI for simulation results including $G(t)$, $P(\tau)$, T_2 dispersion, and intra vs intermolecular relaxation.

As listed in Table 1, heptane in kerogen-IIC yields the longest correlation time $\langle\tau\rangle$, followed by heptane in polymer, then heptane confined in CS1000a. Longer $\langle\tau\rangle$ implies increasing confinement, indicating that kerogen-IIC is the most confining matrix for heptane, followed by the polymer mixture, followed by CS1000a. This can also be deduced from T_1 at low-frequencies (e.g., $f_0 < 2.3$ MHz) where the fast-motion regime relation $T_1 \propto 1/\langle\tau\rangle$ holds, implying that shorter T_1 at $f_0 = 2.3$ MHz indicates increasing confinement (see Table 1). Interestingly, this trend is also reflected in the simulated diffusion coefficient D_{sim} of the confined heptane, which we express in Table 1 in terms of the dimensionless tortuosity $\mathcal{T}$ defined as $D_{bulk}/D_{sim} = \mathcal{T}$, where $D_{bulk} = 3.43\times10^{-9}$ m^2/s is the diffusion coefficient for bulk heptane.[19] Our simulations indicate that increasing confinement, which manifests itself as increasing $\langle\tau\rangle$ and decreasing T_1 at $f_0 = 2.3$ MHz, correlates with the tortuosity $\mathcal{T}$ of the confining medium.

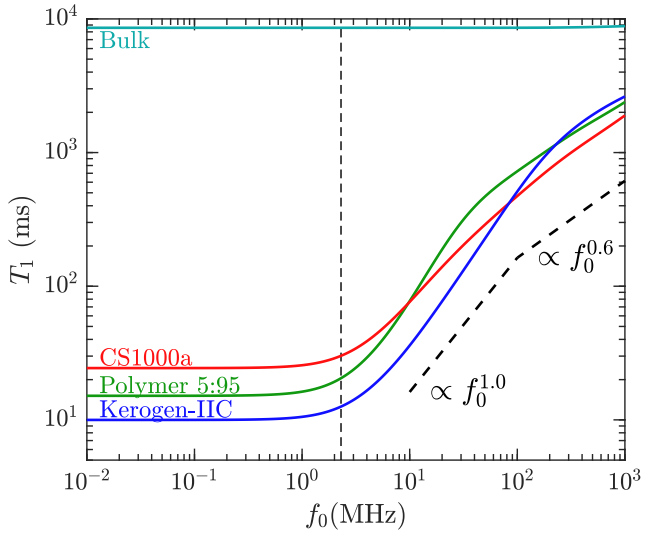


Figure 2: T_1 dispersion for heptane confined in the two models of kerogen studied. The bulk heptane, and heptane confined in poly(isobutene), are also plotted for comparison. The dashed line indicates $f_0 = 2.3$ MHz. The functional forms $T_1 \propto f_0^\beta$ are also plotted.

Fig. 2 shows the computed T_1 dispersion (i.e., frequency dependence), where T_1 shows significant dispersion at higher frequencies

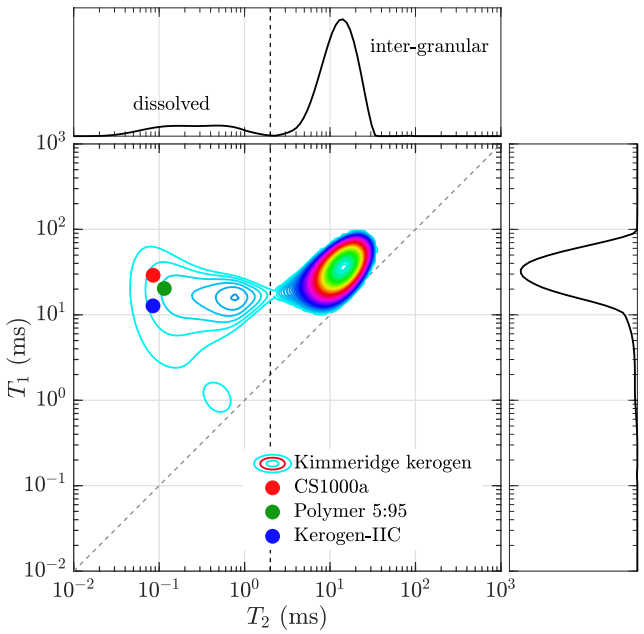


Figure 3: 2D T_1-T_2 map measurement of heptane-saturated kerogen isolates from the Kimmeridge Shale at $f_0 = 2.3$ MHz,[26] T_1 (T_2) projections at the top (right) subplots (respectively), 1-1 diagonal line $T_1 = T_2$, and vertical cutoff line separating dissolved heptane ($T_2 <$ 2 ms) from inter-granular heptane. Also shown are simulation results from Table 1, *without any models or free parameters.*

(f_0 >10 MHz), as expected from our previous work.[19] Specifically, heptane in polymer 5:95 and kerogen-IIC shows approximate $T_1 \propto f_0^1$ behavior between $10 < f_0 < 100$ MHz followed by shallower $T_1 \propto f_0^{0.6}$ behavior above $f_0 > 100$ MHz, consistent with viscous fluids.[12] Meanwhile heptane in CS1000a shows $T_1 \propto f_0^{0.6}$ behavior at $f_0 > 10$ MHz and above. The universal form $T_1 \propto f_0^{0.6}$ above $f_0 > 100$ MHz for all three systems shows the lack of dependence of T_1 on the level of confinement for heptane, analogous to T_1 plateauing at high η/T for viscous fluids. Furthermore, the functional form $T_1 \propto f_0^{0.6}$ is consistent with measurements of heptane confined in organic-rich chalk.[33] In general, a power-law dependence $T_1 \propto f_0^{\beta}$ suggests relaxation by RMTD (reorientations mediated by translational displacements).[34] Further investigations are underway to see whether the dynamic molecular modes $P(\tau)$ can give insights into the RMTD mechanism and the surface topology.

Fig. 3 shows the simulated T_1 values at $f_0 = 2.3$ MHz from Table 1 compared to the 2D T_1-T_2 measurement (also at $f_0 = 2.3$ MHz) of heptane confined in kerogen isolates from Kimmeridge Shale taken from Ref. 26,35,36, which is a Type II immature kerogen. See SI for more details about the experiment. The simulations give consistent values for T_1 compared to the measured signal for dissolved heptane ($T_2 < 2$ ms). The projection of the measured T_1 distribution for dissolved heptane is shown Fig. 4 alongside the simulation results from Table 1. The kerogen-IIC matrix gives the closest match with the log-mean of the measured T_1 distribution ($T_{1LM} \simeq 11$ ms) for dissolved heptane, *without any models or free parameters.* We note that the realistic kerogen model used here provides greater surface area and surface roughness than smooth nano-slits and cylinders.[37,38] This results in much larger confinement effects in kerogen where the low-frequency T_1 is ∼3 orders of magnitude shorter than bulk, compared to a factor ∼2 for smooth nano-surfaces.

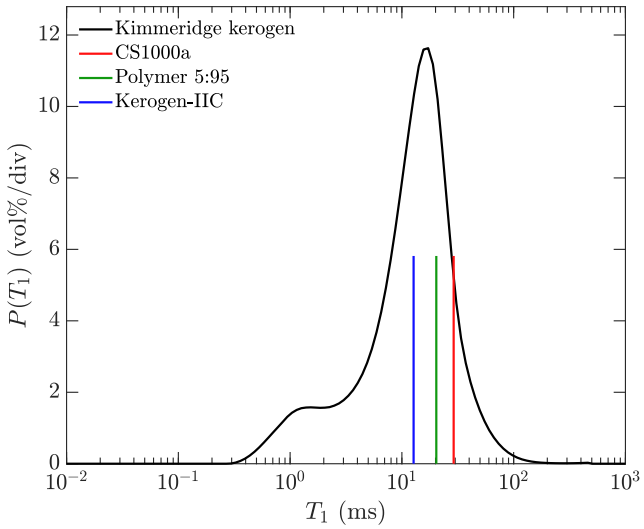


Figure 4: T_1 distribution for heptane-saturated Kimmeridge kerogen, taken from the T_1 projection of Figure 3 for dissolved heptane signal alone ($T_2 < 2$ ms). Also shown are simulation results from Table 1.

T_2 residual dipolar coupling: In the fast-motion (i.e., low-frequency) regime, the simulations would normally predict that $T_2 \simeq T_1$ lies on the 1-1 diagonal of the 2D map, which

is clearly not consistent with T_2 measurements for dissolved heptane in Figure 3. Similar inadequacies in T_2 have also been noted in other nano-confined systems.[39,40] Upon reflection, we can infer that in contrast to the bulk, there is anisotropy in the system originating from strong adsorption onto the kerogen surface, leading to additional dephasing (i.e.. transverse relaxation) in T_2. This residual dipolar coupling (RDC) has been hypothesized to play an important role in organic-rich shale.[41,42] The RDC is given by the following expression:[41]

$$\Delta\omega_{RDC} = \frac{1}{2}\frac{\mu_0}{4\pi}\gamma^2\hbar\times \frac{1}{N_i}\sum_{i=0}^{N_i}\left|\sum_{j\neq i}^{N_j}\left\langle\frac{3\cos^2\theta_{ij}(t)-1}{r_{ij}^3(t)}\right\rangle_t\right| \quad (7)$$

in units of (rad/s), where r_{ij} is the distance between ^{1}H dipoles i and j, and θ_{ij} is the angle the vector connecting the two dipoles make with the external magnetic field. We also compute the RDC for bulk heptane $\Delta\omega_{RDC}^{\text{bulk}}$, then take the difference between confined heptane and bulk to determine $T_{2,RDC}$ as such

$$\frac{1}{T_{2,RDC}} = \Delta\omega_{RDC} - \Delta\omega_{RDC}^{\text{bulk}} \quad (8)$$

SI provides details about the RDC calculations.

As listed in Table 1, we find a comparable $T_{2,RDC} \simeq 0.085$ ms for CS1000a and kerogen-IIC, while $T_{2,RDC} \simeq 0.120$ ms for polymer 5:95 is longer, which may be due to the more flexible nature of polymer 5:95 compared to kerogen-IIC or CS1000a. The $T_{2,RDC} \simeq 0.085$ ms for kerogen-IIC implies a RDC of $\Delta f_{RDC} = 1/(2\pi T_{2,RDC}) \simeq 1900$ Hz, which is $\sim$1 order of magnitude larger than previous reports of heptane confined in 6 nm diameter silica nanotubes $\Delta f_{RDC} \simeq 140$ Hz.[43] The larger Δf_{RDC} for kerogen-IIC is because heptane is completely "adsorbed" in the kerogen, i.e., the nano-pores are of order the size of the heptane molecule, resulting in larger confinement effects than the 6 nm silica nano-tubes.

The distribution of T_2 relaxation times often found in measurements of porous media are due to the distribution in pore-sizes in the sample. In the present case, the relaxation induced by the pore, termed as "surface relaxation" time, is equal to $T_{2,RDC} \simeq 0.085$ ms for kerogen-IIC. The total relaxation rate is given by the sum of the two relaxation rates, with the adsorbed heptane relaxing at $T_{2,RDC}$ (surface), and the pore fluid heptane relaxing at $T_{2,B}$ (bulk), both of which are in fast exchange with each other, i.e. in the fast diffusion regime.[44] Under such conditions the total measured relaxation rate is given by the following expression:[44]

$$\frac{1}{T_2} = \frac{Sh}{V}\frac{1}{T_{2,RDC}+\tau_m} + \left(1-\frac{Sh}{V}\right)\frac{1}{T_{2,B}}, \quad (9)$$

where S is the surface area of the nano-pore, V is the volume of the nano-pore, $h = 0.42$ nm[45] is the thickness of the adsorbed layer of heptane, and τ_m is the residence time of heptane on the kerogen surface. The term Sh/V is essentially the fraction of adsorbed heptane on the surface. Given that $T_{2,RDC} \gg \tau_m$ and that the bulk relaxation term is negligible, we can derive a pore-size distribution from the measured T_2 distribution as such:

$$\frac{1}{T_2} \simeq \frac{h}{T_{2,RDC}}\frac{S}{V} \simeq \rho_2\frac{4}{d}, \quad (10)$$

where we assume the nano-pores to be cylindrical of diameter d, i.e., $S/V = 4/d$. The surface relaxivity parameter $\rho_2 = h/T_{2,RDC} = 4.9$ nm/ms (or 4.9 μm/s, equivalently) is "calibrated" from the simulated $T_{2,RDC}$. This calibration procedure assumes that in the dissolved state, like in the MD simulation cases, all heptanes are completely "adsorbed", hence $Sh/V = 4h/d = 1$ in the simulations. The simulated ρ_2 is consistent with previous reports in organic-rich shale calibrated from scanning electron microscopy (SEM) images.[46]

Fig. 5 shows the pore-size distribution $P(d)$ of dissolved heptane, obtained using Eq. 10 with ρ_2 calibrated from simulations. It is remarkable that $P(d)$ has the potential to provide an accurate pore-size distribution of the organic nano-pores in kerogen from NMR relaxation measurements and MD simulations alone, without any external experimental data to calibrate the NMR pore-size distribution such as SEM im-

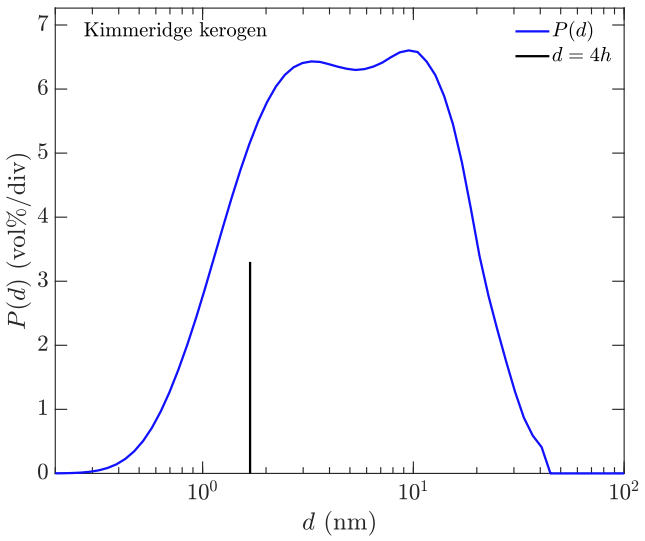


Figure 5: Pore-size distribution $P(d)$ of dissolved heptane in the Kimmeridge kerogen from the T_2 projection (below $T_2 < 2$ ms) in Figure 3, where the pore diameter $d = 4\rho_2 T_2$. The surface relaxivity $\rho_2 = h/T_{2,RDC}$ is calibrated from simulations, with the calibration point $d = 4h$ (i.e., $T_2 = T_{2,RDC}$) shown.

ages or N_2 gas adsorption (BET) isotherms.

A similar derivation of pore-size distribution from T_1 is not presented due to strong cross-relaxation effects in T_1,[33] which are not present in T_2. Cross-relaxation has a tendency to average out and narrow the T_1 distribution from all ^{1}H in contact with each other through spin diffusion (a.k.a. magnetization transfer).[16,39,40,42,47] In the present case, the ^{1}H bearing molecules in contact with each other include inter-granular heptane, dissolved heptane, bitumen, and kerogen. Note that cross-relaxation is independent of the fact that the bitumen and kerogen are not detectable here due to their fast solid-like $T_{2G} \simeq 0.01$ ms relaxation and instrumental limitations at low frequencies $f_0 = 2.3$ MHz (typically, higher frequency relaxometers with shorter dead-times are required to detect solid-like signals[33,48]). Cross-relaxation in the present case is evidenced by the narrower T_1 distribution compared to T_2 in Fig. 3, which makes the pore-size distribution $P(d)$ more accurate from T_2 than from T_1. On the other hand, the dispersion in T_1 allows for a wealth of information about the dynamic molecular modes in $P(\tau)$, making the T_1-T_2 correlation a very powerful combination for fluids under nano-confinement.

In summary, we use MD simulations of heptane confined in realistic kerogen models to compute the NMR ^{1}H-^{1}H dipole-dipole relaxation including T_1 relaxation dispersion and T_2 residual dipolar coupling. We find that heptane T_1 relaxation is strongly enhanced by confinement in organic nano-pores, with T_1 at low-frequencies reduced by $\sim$3 orders of magnitude compared to bulk. The simulated T_1 values agree with the measurements of heptane in kerogen from the Kimmeridge Shale, *without any models or free parameters.* We find that the T_2 relaxation is dictated by residual dipolar coupling, with T_2 reduced by $\sim$5 orders of magnitude compared to bulk. We use the simulated T_2 to calibrate the surface relaxivity ρ_2, which is used to convert the measured T_2 distribution of dissolved heptane into the pore-size distribution $P(d)$ of the organic nano-pores in kerogen, *without additional experimental data.* Importantly, the measurements of heptane confined in kerogen can be explained by ^{1}H-^{1}H dipole-dipole relaxation, without invoking the physics of paramagnetism. Furthermore, our simulation techniques (detailed in the SI) are relevant to ^{1}H-^{1}H dipole-dipole relaxation for all nano-confined systems.

Supporting Information

The Supporting Information includes (1) simulation methodology, (2) additional simulation results, specifically the simulated autocorrelation functions, T_2 dispersion, and separation of intra- and inter-molecular contributions, (3) residual dipolar coupling methodology, and (4) experimental details.

Acknowledgements

We thank Chevron Energy Technology Company, the Rice University Consortium on Processes in Porous Media, and the American Chemical Society Petroleum Research Fund (No. ACS PRF 58859-ND6) for financial support. We gratefully acknowledge the National

Energy Research Scientific Computing Center, which is supported by the Office of Science of the U.S. Department of Energy (No. DE-AC02-05CH11231) and the Texas Advanced Computing Center (TACC) at The University of Texas at Austin for high-performance computer time and support. Research at Oak Ridge National Laboratory is supported under contract DE-AC05-00OR22725 from the U.S. Department of Energy to UT-Battelle, LLC. This research used resources of National Energy Research Scientific Computing Center, which is supported by the Office of Science of the U.S. Department of Energy under Contract # DE-AC02-05CH11231. ORNL Pub. ID. 188552.

References

(1) Yethiraj, A.; Striolo, A. Fracking: What Can Physical Chemistry Offer? *J. Phys. Chem. Lett.* **2013**, *4*, 687–690.

(2) Hosseininoosheri, P.; Hosseini, S.; nez López, V. N.; Lake, L. Impact of Field Development Strategies on CO_2 Trapping Mechanisms in a CO_2–EOR Field: A Case Study in the Permian Basin (SACROC unit). *Int. J. Greenhouse Gas Control* **2018**, *72*, 92–104.

(3) Bloembergen, N.; Purcell, E. M.; Pound, R. V. Relaxation Effects in Nuclear Magnetic Resonance Absorption. *Phys. Rev.* **1948**, *73*, 679–712.

(4) Torrey, H. C. Nuclear Spin Relaxation by Translational Diffusion. *Phys. Rev.* **1953**, *92*, 962–969.

(5) Vinegar, H. J.; Tutunjian, P. N.; Edelstein, W. A.; Roemer, P. B. Whole-Core Analysis by ^{13}C NMR. *Soc. Petrol. Eng. J.* **1991**, *6*, 183–189.

(6) LaTorraca, G. A.; Stonard, S. W.; Webber, P. R.; Carlson, R. M.; Dunn, K. J. Heavy Oil Viscosity Determination Using NMR Logs. *Soc. Petrophys. Well Log Analysts* **1999**, SPWLA–1999–PPP.

(7) Zhang, Y.; Hirasaki, G. J.; House, W. V.; Kobayashi, R. Oil and Gas NMR Properties: the Light and Heavy Ends. *Soc. Petrophys. Well Log Analysts* **2002**, *SPWLA-2002-HHH*.

(8) Yang, Z.; Hirasaki, G. J. NMR Measurement of Bitumen at Different Temperatures. *J. Magn. Reson.* **2008**, *192*, 280–293.

(9) Yang, Z.; Hirasaki, G. J.; Appel, M.; Reed, D. A. Viscosity Evaluation for NMR Well Logging of Live Heavy Oils. *Petrophysics* **2012**, *53*, 22–37.

(10) Kausik, R.; Freed, D.; Fellah, K.; Feng, L.; Ling, Y.; Simpson, G. Frequency and Temperature Dependence of 2D NMR T_1-T_2 Maps of Shale. *Petrophysics* **2019**, *60*, 37–49.

(11) Singer, P. M.; Chen, Z.; Alemany, L. B.; Hirasaki, G. J.; Zhu, K.; Xie, Z. H.; Vo, T. D. Interpretation of NMR Relaxation in Bitumen and Organic Shale Using Polymer-Heptane Mixes. *Energy Fuels* **2018**, *32*, 1534–1549.

(12) Singer, P. M.; Valiya Parambathu, A.; Wang, X.; Asthagiri, D.; Chapman, W. G.; Hirasaki, G. J.; Fleury, M. Elucidating the ^{1}H NMR Relaxation Mechanism in Polydisperse Polymers and Bitumen using Measurements, MD Simulations, and Models. *J. Phys. Chem. B* **2020**, *124*, 4222–4233.

(13) Serve, O.; Choblet, H.; Livadaris, V.; Korb, J.-P. Probing Hydrocarbon Dynamics at Asphaltene/Maltene Interfaces for the Global Characterization of Bitumen. *J. Colloid Interface Sci.* **2021**, *593*, 21–31.

(14) Stukowski, A. Visualization and Analysis of Atomistic Simulation Data with OVITO - the Open Visualization Tool. *Model Simul. Mat. Sci. Eng.* **2009**, *18*, 015012.

(15) Singer, P. M.; Asthagiri, D.; Chapman, W. G.; Hirasaki, G. J. Molecular Dynamics Simulations of NMR Relaxation and Diffusion of Bulk Hydrocarbons and Water. *J. Magn. Reson.* **2017**, *277*, 15–24.

(16) Singer, P. M.; Asthagiri, D.; Chen, Z.; Valiya Parambathu, A.; Hirasaki, G. J.; Chapman, W. G. Role of Internal Motions and Molecular Geometry on the NMR Relaxation of Hydrocarbons. *J. Chem. Phys.* **2018**, *148*, 164507.

(17) Singer, P. M.; Asthagiri, D.; Chapman, W. G.; Hirasaki, G. J. NMR Spin-Rotation Relaxation and Diffusion of Methane. *J. Chem. Phys.* **2018**, *148*, 204504.

(18) Asthagiri, D.; Chapman, W. G.; Hirasaki, G. J.; Singer, P. M. NMR ^{1}H–^{1}H Dipole Relaxation in Fluids: Relaxation of Individual ^{1}H–^{1}H Pairs versus Relaxation of Molecular Modes. *J. Phys. Chem. B* **2020**, *124*, 10802–10810.

(19) Valiya Parambathu, A.; Singer, P. M.; Hirasaki, G. J.; Chapman, W. G.; Asthagiri, D. Critical Role of Confinement in the NMR Surface Relaxation and Diffusion of *n*-heptane in a Polymer Matrix Revealed by MD Simulations. *J. Phys. Chem. B* **2020**, *124*, 3801–3810.

(20) Singer, P. M.; Parambathu, A. V.; Pinheiro dos Santos, T. J.; Liu, Y.; Alemany, L. B.; Hirasaki, G. J.; Chapman, W. G.; Asthagiri, D. Predicting ^{1}H NMR Relaxation in Gd^{3+}-Aqua using Molecular Dynamics Simulations. *Phys. Chem. Chem. Phys.* **2021**, *23*, 20974–20984.

(21) Pinheiro dos Santos, T. J.; Parambathu, A. V.; Walsh, C. C. F. C.; Greenbaum, S. G.; Chapman, W. G.; Asthagiri, D.; Singer, P. M. Thermal and Concentration Effects on ^{1}H NMR Relaxation of Gd^{3+}-Aqua using MD Simulations and Measurements. *Phys. Chem. Chem. Phys.* **2023**,

(22) Jain, S. K.; Pellenq, R. J.-M.; Pikunic, J. P.; Gubbins, K. E. Molecular Modeling of Porous Carbons Using the Hybrid Reverse Monte Carlo Method. *Langmuir* **2006**, *22*, 9942–9948.

(23) Falk, K.; Coasne, B.; Pellenq, R.; Ulm, F. J.; Bocquet, L. Subcontinuum Mass Transport of Condensed Hydrocarbons in Nanoporous Media. *Nat. Commun.* **2015**, *6*, 1–7.

(24) Collell, J.; Ungerer, P.; Galliero, G.; Yiannourakou, M.; Montel, F.; Pujol, M. Molecular Simulation of Bulk Organic Matter in Type II Shales in the Middle of the Oil Formation Window. *Energy Fuels* **2014**, *28*, 7457–7466.

(25) Ungerer, P.; Collell, J.; Yiannourakou, M. Molecular Modeling of the Volumetric and Thermodynamic Properties of Kerogen: Influence of Organic Type and Maturity. *Energy Fuels* **2015**, *29*, 91–105.

(26) Singer, P. M.; Chen, Z.; Wang, X.; Hirasaki, G. J. Diffusive Coupling in Heptane-Saturated Kerogen Isolates Evidenced by NMR T_1-T_2 and T_2-T_2 Maps. *Fuel* **2020**, *280*, 118626.

(27) Abragam, A. *Principles of Nuclear Magnetism*; Oxford University Press, International Series of Monographs on Physics, 1961.

(28) McConnell, J. *The Theory of Nuclear Magnetic Relaxation in Liquids*; Cambridge University Press, 1987.

(29) Cowan, B. *Nuclear Magnetic Resonance and Relaxation*; Cambridge University Press, 1997.

(30) Faux, D. A.; McDonald, P. J.; Howlett, N. C.; Bhatt, J. S.; Churakov, S. V. Nuclear Magnetic Resonance Relaxometry of Water in Two and Quasi-Two Dimensions. *Phys. Rev. E* **2013**, *87*, 062309.

(31) Singer, P. M.; Arsenault, A.; Imai, T.; Fujita, M. ^{139}La NMR Investigation of the Interplay Between Lattice, Charge, and Spin Dynamics in the Charge-Ordered High-T_c Cuprate $La_{1.875}Ba_{0.125}CuO_4$. *Phys. Rev. B* **2020**, *101*, 174508.

(32) Wang, J.; Yuan, W.; Singer, P. M.; Smaha, R. W.; He, W.; Wen, J.; Lee, Y. S.; Imai, T. Emergence of Spin Singlets with Inhomogeneous Gaps in the Kagome Lattice Heisenberg Antiferromagnets Zn-Barlowite and Herbertsmithite. *Nature Physics* **2021**, *17*, 1109–1113.

(33) Liu, Y.; Wang, X.; Hirasaki, G. J.; Vinegar, E. V.; Vinegar, H. G.; Singer, P. M. Separation of Solid and Liquid Components in Organic-Rich Chalks Using NMR Relaxation. *Fuel* **2023**, *333*, 126223.

(34) Gizatullin, B.; Mattea, C.; Shikhov, I.; Arns, C.; Stapf, S. Modeling Molecular Interactions with Wetting and Non-Wetting Rock Surfaces by Combining Electron Paramagnetic Resonance and NMR Relaxometry. *Langmuir* **2022**, *38*, 11033–11053.

(35) Singer, P. M.; Chen, Z.; Hirasaki, G. J. Fluid Typing and Pore Size in Organic Shale Using 2D NMR in Saturated Kerogen Isolates. *Petrophysics* **2016**, *57*, 604–619.

(36) Chen, Z.; Singer, P. M.; Kuang, J.; Vargas, M.; Hirasaki, G. J. Effects of Bitumen Extraction on the 2D NMR Response of Saturated Kerogen Isolates. *Petrophysics* **2017**, *58*, 470–484.

(37) Mutisya, S. M.; Kirch, A.; de Almeida, J. M.; Sánchez, V. M.; Miranda, C. R. Molecular Dynamics Simulations of Water Confined in Calcite Slit Pores: An NMR Spin Relaxation and Hydrogen Bond Analysis. *J. Phys. Chem. C* **2017**, *121*, 6674–6684.

(38) Amaro-Estrada, J. I.; Wang, Y.; Torres-Verdín, C. Quantifying the Effect of Spatial Confinement on the Diffusion and Nuclear Magnetic Resonance Relaxation of Water/Hydrocarbon Mixtures: A Molecular Dynamics Simulation Study. *Langmuir* **2022**,

(39) Chen, J.-H.; Haghmoradi, A.; Althaus, S. M. NMR Intermolecular Dipolar Cross-Relaxation in Nanoconfined Fluids. *J. Phys. Chem. B* **2020**, *124*, 10237–10244.

(40) Chen, J.-H.; Liu, C.; Althaus, S. M.; Boudjatit, M. Nuclear Magnetic Resonance Dipolar Cross-Relaxation Interaction between Nanoconfined Fluids and Matrix Solids. *ACS Omega* **2022**, doi.org/10.1021/acsomega.2c05639.

(41) Washburn, K. E.; Cheng, Y. Detection of Intermolecular Homonuclear Dipolar Coupling in Organic Rich Shale by Transverse Relaxation Exchange. *J. Magn. Reson.* **2017**, *278*, 18–24.

(42) Washburn, K. E. Relaxation Mechanisms and Shales. *Concepts Magn. Reson.* **2014**, *A 43*, 57–78.

(43) Valiullin, R.; Khokhlov, A. Orientational Ordering of Linear *n*-Alkanes in Silicon Nanotubes. *Physical Review E* **2006**, *73*, 051605.

(44) Brownstein, K. R.; Tarr, C. E. Importance of Classical Diffusion in NMR Studies of Water in Biological Cells. *Phys. Rev. A* **1979**, *19*, 2446–2453.

(45) Mao, Z.; Sinnott, S. B. Separation of Organic Molecular Mixtures in Carbon Nanotubes and Bundles: Molecular Dynamics Simulations. *J. Phys. Chem. B* **2001**, *105*, 6916–6924.

(46) Rylander, E.; Singer, P. M.; Jiang, T.; Lewis, R. E.; McLin, R.; Sinclair, S. M. NMR T_2 Distributions in the Eagle Ford Shale: Reflections on Pore Size. *Soc. Petrol. Eng.* **2013**, *SPE-164554-MS*.

(47) Gerig, J. Cross Relaxation in Liquid Methanol. *J. Magn. Reson.* **2011**, *210*, 171–176.

(48) Zamiri, M. S.; MacMillan, B.; Marica, F.; Guo, J.; Romero-Zerón, L.; Balcom, B. J. Petrophysical and Geochemical Evaluation of Shales Using Magnetic Resonance T_1-T_2^* Relaxation Correlation. *Fuel* **2021**, *284*, 119014.

arXiv:2212.02489v1 [physics.chem-ph] 5 Dec 2022

Supporting Information for:

Effect of Nano-Confinement on NMR Relaxation of Heptane in Kerogen from MD Simulations and Measurements

Arjun Valiya Parambathu,[†,‡] Walter G. Chapman,[†] George J. Hirasaki,[†]

Dilip Asthagiri,[*,¶] and Philip M. Singer[*,†]

†*Department of Chemical and Biomolecular Engineering, Rice University, 6100 Main St., Houston, TX 77005, USA*

‡*Department of Chemical and Biomolecular Engineering, 150 Academy St, University of Delaware, Newark, DE 19716, USA*

¶*Oak Ridge National Laboratory, 1 Bethel Valley Road, Oak Ridge, TN 37830-6012*

E-mail: asthagiridn@ornl.gov; ps41@rice.edu

Contents

S.1 Simulation methodology **S2**

S.1.1 Heptane in mesoporous carbon matrix S2

S.1.1.1 Matrix structure S2

S.1.1.2 Grand canonical Monte Carlo simulations S3

S.1.1.3 Molecular Dynamics simulations S3

S.1.2 Heptane in Kerogen II-C Model S4

S.1.2.1 Matrix structure and MD simulation details S4

S.1.2.2 Creating the initial structure S4

S.1.3 Diffusion coefficient S6

S.2 Additional simulation results **S8**

S.2.1 Autocorrelation of dipole-dipole relaxation S8

S.2.2 Intra vs Intermolecular relaxation S11

S.2.3 T_2 dispersion S12

S.3 Residual dipolar coupling methodology **S14**

S.4 Experimental details **S16**

References **S19**

S.1 Simulation methodology

S.1.1 Heptane in mesoporous carbon matrix

S.1.1.1 Matrix structure

We used the CS1000a mesoporous carbon matrix as an idealization of the kerogen system.[1] The matrix itself is rigid, but interestingly the pore distribution is similar to that in Marcellus Kerogen and gives a good description of diffusivity for alkanes in kerogen under reservoir conditions.[2] The carbon atoms forming the wall are modeled after graphene carbon atom with 12-6 Lennard-Jones $\sigma = 3.550$ Å and $\epsilon = 35.222$ kJ/mol.

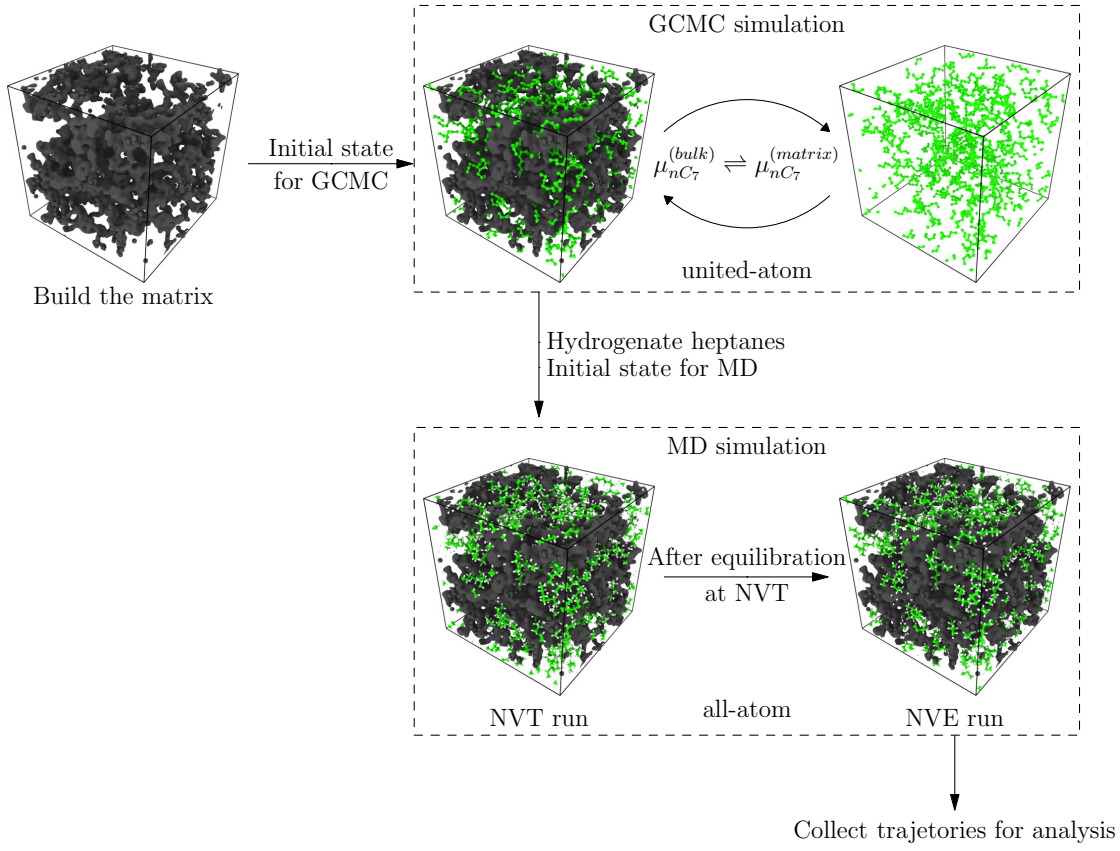


Figure S1: Schematic of the simulation details for heptane in cs1000a carbon matrix.

S.1.1.2 Grand canonical Monte Carlo simulations

The CS1000a matrix was populated with heptane using the grand canonical Monte Carlo simulation technique using Cassandra.[3] The system was equilibrated with a bulk heptane system corresponding to 298 K and 1 atm. The configurational bias technique was used to improve the sampling.[4] We simplified the MC simulation by opting for a united atom force field in this step. The heptane was modeled using TraPPE force field.[5] The system was equilibrated for 1×10^5 steps, and then the data was collected over a subsequent run of 3×10^6 steps. The number of molecules in the system was observed to be stable at 249 molecules. We use the last configuration for further exploration using molecular dynamics.

S.1.1.3 Molecular Dynamics simulations

We use NAMD[6,7] to perform the molecular dynamics simulations. In this phase, we explicitly describe hydrogens, which were added using the PSFGEN tool to the previously saved united atom heptane configuration. In other words, we assume each matrix carbon atom as a site for ^{1}H dipole relaxation. The heptanes are described using the CHARMM General Force Field.[8] The CS1000a matrix was modeled using 12-6 Lennard-Jones sphere with $\sigma = 3.550$ Å and $\epsilon = 35.222$ kJ/mol, exactly as the GCMC simulations. The Lennard-Jones interactions were terminated at 14 Å with smooth switching from 13 Å. The Coulombic interactions were cutoff at 13 Å, and we use the particle mesh Ewald procedure to describe long-range electrostatic interactions. We minimized the system to remove any strain using the conjugate gradient method. The equations of motion were propagated using the RESPA multistep algorithm with a base time step of 1 fs. The system was equilibrated at a constant temperature of 298.15 K for 1 ns. The temperature was controlled by reassigning velocities (obtained from a Maxwell-Boltzmann distribution) every 250 fs. The thermostat was then turned off and the production was carried out for 5 ns.

S.1.2 Heptane in Kerogen II-C Model

S.1.2.1 Matrix structure and MD simulation details

The molecular model for different types of kerogen at different maturities was developed by Ungerer *et al.*[9] In this study, we use Kerogen II-C model, which is an oil prone mature kerogen from marine shales. The H/C ratio for this kerogen is 0.90 and the O/C ratio is 0.05. We use LAMMPS[10,11] to perform the molecular dynamics simulations. The PCFF+ force field[12] (an extension of PCFF[13]) was used to model the system. The parameters were obtained from MedeA® software environment[14] and Collel *et al.*[15] The Lennard-Jones and Coulombic interactions were terminated at 15 Å. We use the particle-particle particle-mesh procedure to describe the long range electrostatic interactions. The equations of motions were propogated using the velocity Verlet alogirthm with a timestep of 1 fs. For equilibration runs, the temperature and pressures were controlled using a three chained Nosé-Hoover thermostat[16,17] and a Nosé-Hoover barostat[18] respectively.

S.1.2.2 Creating the initial structure

In order to populate the matrix at approximately the right thermodynamic conditions, we use the simulated annealing technique. We create 8 copies of kerogen molecule and N copies of heptane, and pack them at a very low density (0.1 g/cm^3) using in-built tools in LAMMPS. We next compress the mixture to obtain the target density. We turn off the long-range electrostatics and use a LJ and Coulombic cutoffs of 9 Å, since only short-range interactions are critical in molecular packing. We then perform an NVT simulation at 1000 K for 100 ps. This step ensures reasonable mixing of the system and removes any biases created while making the initial structure. This is followed by NPT simulations of 200 ps to compress the system to 100 atm. We then slowly reduce the temperatures from 900 K to 300 K in 4 steps of 200 ps. We then restore the long-range electrostatics, and change the LJ and Coulombic cutoffs to 15 Å. Then we equilibrated the system for 1 ns at the required

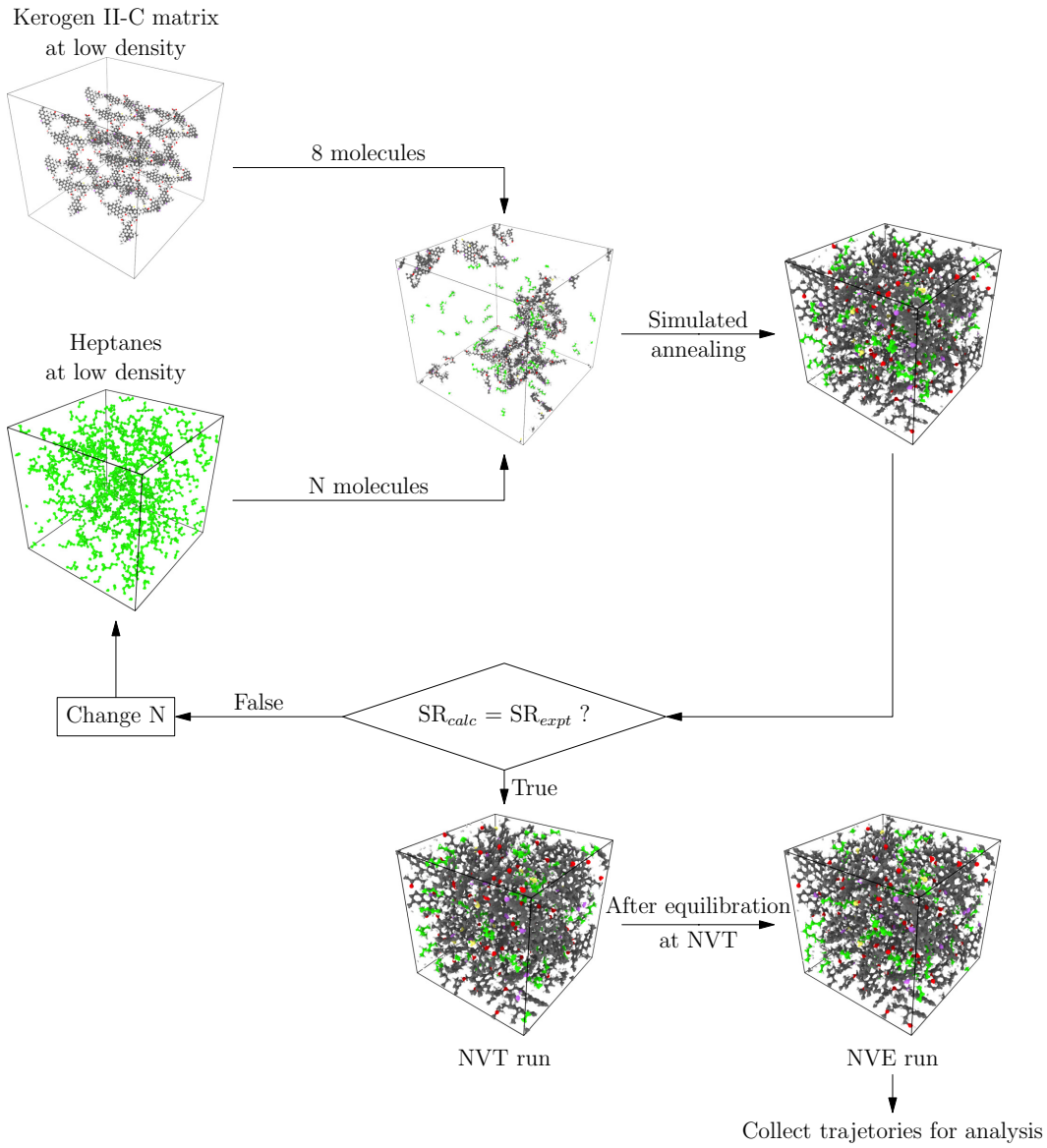


Figure S2: Schematic of the simulation details for heptane in kerogen II-C. Note that, unlike heptane in CS1000a system where we used a GCMC simulations to create the initial structure, we utilize experimental estimate of dissolved heptane to estimate the initial structure.

state of 298.15 K and 1 atm pressure.

The number of heptanes was changed from 20 molecules to 100 molecules. We found that 40 molecules of heptane gave us the right swelling ratio for the given kerogen model.

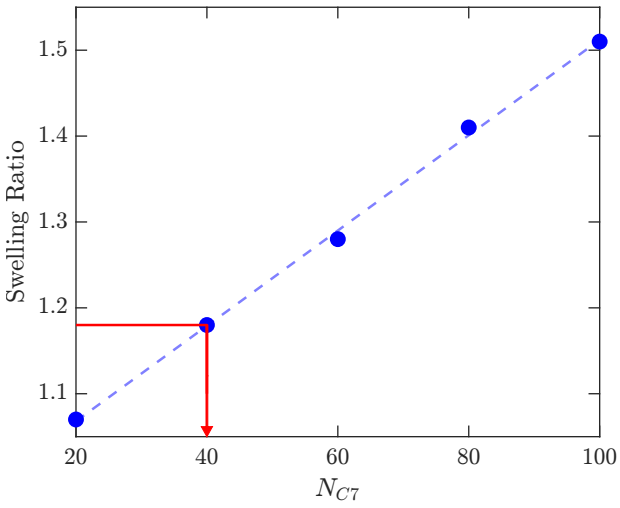


Figure S3: Swelling ratio for different number of heptane molecule. The estimate for heptane swelling ratio in kerogen II-C due to dissolved heptane is 1.18.[19]

Note that the swelling ratio $SR = 1.18$ can also be expressed as a volume percent heptane

$$\phi_\mu = 100\left(1 - \frac{1}{SR}\right) \quad \text{(vol\%)}, \tag{S.1}$$

yielding $\phi_\mu = 15.2$ vol%, which is consistent with the measurement of $\phi_\mu = 13.6$ vol%. The system with 40 heptane molecules in 8 molecules of Kerogen-IIC was simulated for production for 10 ns at constant energy.

S.1.3 Diffusion coefficient

The diffusion coefficient was computed using Einstein relation

$$D_{sim} = \lim_{t\to\infty} \frac{1}{6} \frac{\delta\langle \Delta r^2 \rangle}{\delta t} \tag{S.2}$$

where $\delta\langle \Delta r^2 \rangle$ is the mean-square displacement of the center-of-mass of the heptane as a function of evolution time t. We sample all the heptanes in each of the matrix to compute the diffusion coefficient, and evaluated for diffusion evoultion time of 1 ns. Note that we do not apply the finite system size corrections here as an estimate of viscosity is required,[20]

which is ill-defined for a rigid matrix system. Our previous study on heptane-polymer matrix indicate that at the correction is ∼9% for heptane in bulk D_{bulk}, and decreases to ∼2% for the polymer 5:95 system.

Table S1: Self-diffusion coefficient of heptanes using Eq. S.2, along with corresponding tortuosity values $\mathcal{T} = D_{bulk}/D_{sim}$.

Confining matrix	D_{sim} ($m^2s^{-1}/10^{-11}$)	$\mathcal{T}$ (–)
Bulk	343	1
CS1000a	4.27	80
Polymer 5:95	1.05	320
Kerogen-IIC	0.93	370

The tortuosity $\mathcal{T}$ defined as $\mathcal{T} = D_{bulk}/D_{sim}$ assumes that heptane is in the tortuosity limit, which is valid for dissolved heptane.

S.2 Additional simulation results

S.2.1 Autocorrelation of dipole-dipole relaxation

The autocorrelation $G(t)$ can be applied to all ^{1}H's taken together or grouped according to whether the two protons are on the same molecule, leading to *intra*molecular relaxation, or on separate molecules, leading to *inter*molecular relaxation, see Fig. S4. Such a partitioning is valid if there is no cross coupling between the two relaxation mechanisms, as is the case here. We indicate *intra*molecular relaxation by the subscript R and *inter*molecular relaxation

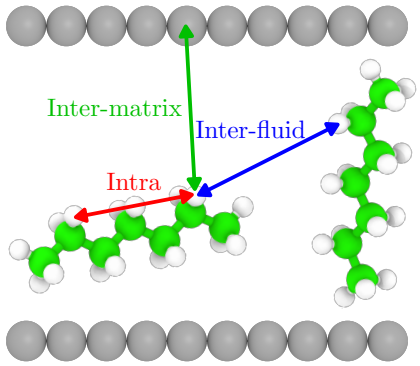


Figure S4: Partitioning into *intra*molecular relaxation $G_R(t)$, and *inter*molecular relaxation $G_T(t)$. Note that *inter*molecular relaxation consists of both other heptanes and the matrix.

by the subscript T. We follow Eq. 2 to 6 to obtain $T_{1,R}$ and $T_{1,T}$. The total relaxation is then given as

$$\frac{1}{T_1} = \frac{1}{T_{1R}} + \frac{1}{T_{1T}}. \tag{S.3}$$

The *intra*molecular and *inter*molecular autocorrelation functions $G_{R,T}(t)$ were computed using Eq. 1 from the last 6.5536 ns of the simulations, and upto lag time of $t_{max} = 3$ ns is utilized. It should be noted that for CS1000a the matrix is made of carbon atoms alone, hence the matrix effect was computed assuming each carbon atom as a site for a ^{1}H dipole. This is included in the *inter*molecular autocorrelation calculations. The direction of the magnetic field $\vec{B}_0$ was chosen to be the three primary axes $\vec{x}$, $\vec{y}$, and $\vec{z}$, and the mean $G_{R,T}(t)$

was taken for further analysis. The computed autocorrelations are shown in Fig. S5.

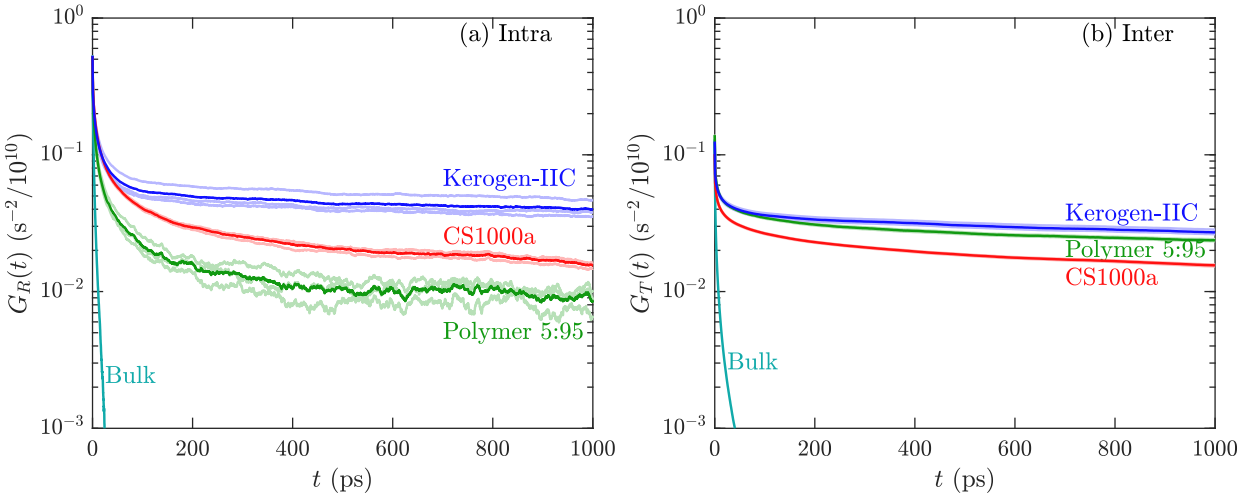


Figure S5: (a) *Intra*molecular autocorrelation $G_R(t)$ and (b) *inter*molecular autocorrelation $G_T(t)$ for heptane in CS1000a, polymer 5:95, and kerogen-IIC. The darker shade indicates the average $G_{RT}(t)$,and the lighter shades indicates the autocorrelation curve for different directions. The bulk $G_{RT}(t)$ is plotted for comparison.

The distribution of correlation times $P_{RT}(\tau)$ was evaluated using Eq. 3, with $\tau_{min} = 10^{-2}$ ps, $\tau_{max} = 10\,t_{max} = 30$ ns, and fixed regularization parameter $\alpha = 1$.[21,22] The computed distributions are shown in Fig. S6.

We termed the "peaks" observed in the $P(\tau)$ distribution as molecular modes, as it is empirically observed to be functions of molecular structure and its environment. Note that the two shaded areas are the T_1 filters at 2.3 MHz and 400 MHz respectively. T_1 filter signifies the "weight" of a given correlation time towards T_1 at a given frequency. The T_1 filter $\mathcal{L}$ for given frequency ω_0 is given by

$$\mathcal{L}(\omega_0) \propto \left[\frac{2\tau}{1+(\omega_0\tau)^2} + \frac{8\tau}{1+(2\omega_0\tau)^2}\right]. \tag{S.4}$$

We can see that, as the frequency increases, the lower molecular modes are more important. This also highlights that simulations capture NMR relaxation at higher frequencies more accurately. This is an important uncertainity in our results of T_1 values at 2.3 MHz.

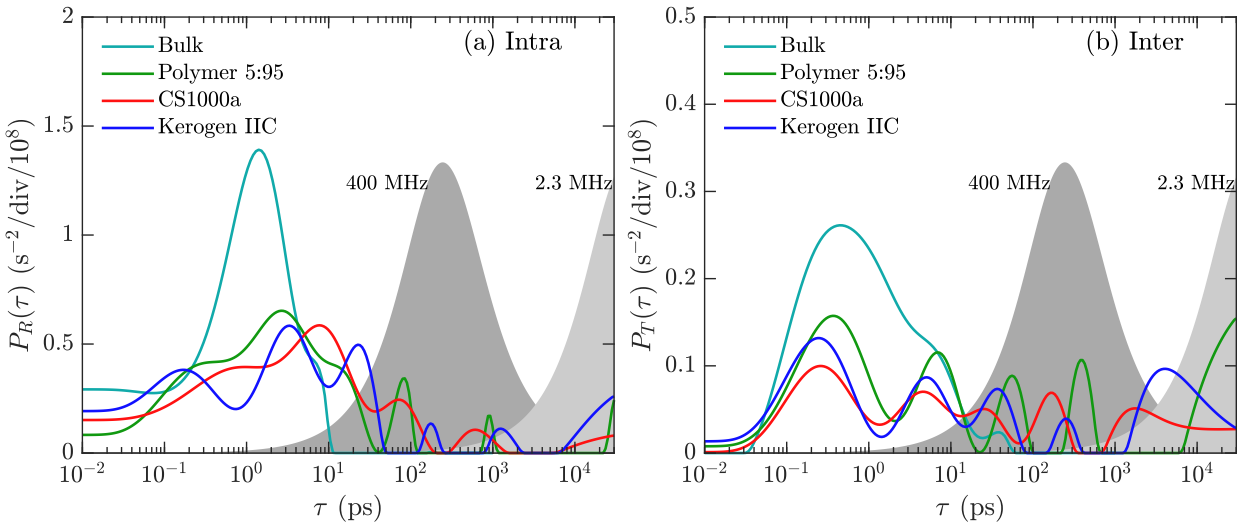


Figure S6: Probability distribution of correlation times for (a) *intra*molecular autocorrelation $P_R(\tau)$ and (b) *inter*molecular autocorrelation $P_T(\tau)$ for heptane in CS1000a, polymer 5:95, and kerogen-IIC. The bulk $P_{RT}(\tau)$ is plotted for comparison. The gray area plot shows the T_1 filter $\mathcal{L}$ at frequencies 2.3 MHz and 400 MHz respectively.

S.2.2 Intra vs Intermolecular relaxation

The effect of the matrix can be elucidated by looking at the individual components of relaxation. Fig. S7 shows the ratio of $T_{1,R}$ relaxation in total relaxation T_1.

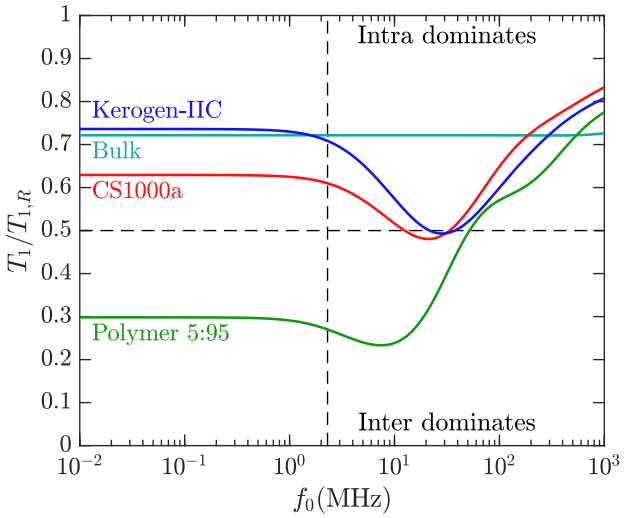


Figure S7: The ratio of *intra*molecular relaxation rate to the total relaxation rate, where $T_1/T_{1R} > 0.5$ indicates that *intra*molecular dominates, while $T_1/T_{1R} < 0.5$ indicates that *inter*molecular dominates. The vertical dashed line indicates the frequency of 2.3 MHz.

Fig. S7 indicates that at low-frequencies ($f_0 \ll 2.3$ MHz), the int*ra*molecular relaxation T_{1R} plays a more significant role in heptane confined in kerogen-IIC and CS1000a compared to polymer. This is due to higher rigidity of the kerogen-IIC and CS1000a matrices compared to the polymer matrix, which considerably affects the int*ra*molecular motion of the heptane molecule. At higher frequencies ($f_0 \gg 100$ MHz), the int*er*molecular contribution diminishes faster than the int*ra*molecular. This can be explained by the T_1 filter on $P_{RT}(\tau)$ distribution, with greater importance to shorter molecular modes at higher frequencies[22] and for $\tau < 10^3$ ps, $P_R(\tau) > P_T(\tau)$.

S.2.3 T_2 dispersion

T_2 for ^{1}H-^{1}H dipole-dipole relaxation is given by:[23,24]

$$\frac{1}{T_2} = \frac{3}{2}J(0) + \frac{5}{2}J(\omega_0) + J(2\omega_0), \tag{S.5}$$

which predicts a mild increase of 10/3 in T_2 with increasing $\omega_0\langle\tau\rangle$. However, all experimental data indicates that the factor 10/3 increase in T_2 is not observed in viscous fluids, and that T_2 remains frequency independent.[21]

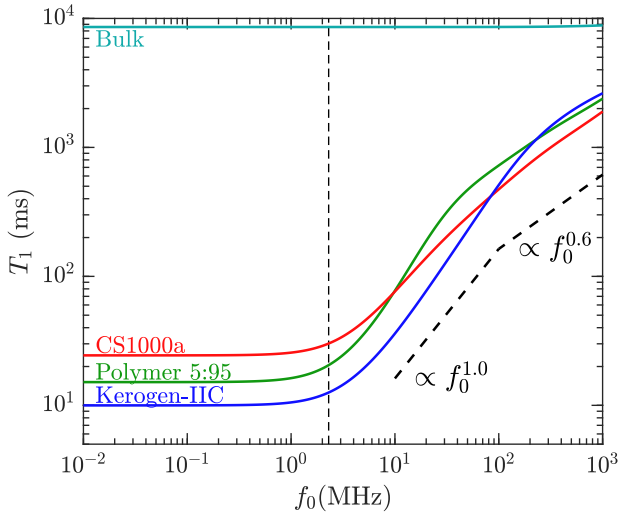


Figure S8: NMR relaxation times T_2 for heptane in the two models of kerogen studied. The bulk heptane and heptane confined in poly(isobutene) are plotted for comparison.

The total transverse relaxation $T_{2,Total}$ is given by the sum of rates of Eq. S.5 and S.7 as such:

$$\frac{1}{T_{2,Total}} = \frac{1}{T_2} + \frac{1}{T_{2,RDC}}. \tag{S.6}$$

For confined heptane, the T_2 term is neglected since T_2 is ~2 orders of magnitude longer than $T_{2,RDC}$, i.e., $T_{2,Total} \simeq T_{2,RDC}$. A comparison of the "$T_2$ dispersion" term versus $T_{2,RDC}$ is shown in Figure S9.

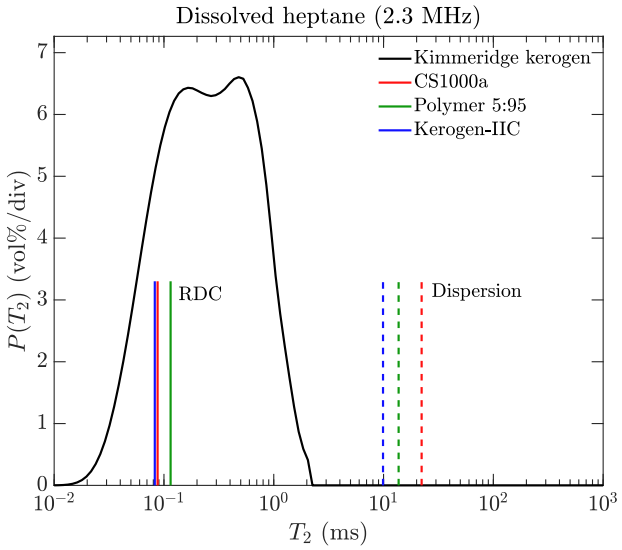


Figure S9: T_2 distribution for heptane-saturated kerogen isolates from the Kimmeridge Shale at $f_0 = 2.3$ MHz, taken from the T_2 projection of Figure 3 for dissolved heptane signal alone ($T_2 < 2$ ms). Also shown are simulation results according to RDC from Eq. S.7 (solid lines) and T_2 dispersion from Eq. S.5 (dashed lines), *without any models or free parameters.*

S.3 Residual dipolar coupling methodology

The residual dipolar coupling $\Delta\omega_{RDC}$[25] is calculated using Eq. 7 (main text) and reproduced here below

$$\Delta\omega_{RDC} = \frac{1}{2}\frac{\mu_0}{4\pi}\gamma^2\hbar\frac{1}{N_i}\sum_{i=0}^{N_i}\left|\sum_{j\neq i}^{N_j}\left\langle\frac{3\cos^2\theta_{ij}(t)-1}{r_{ij}^3(t)}\right\rangle_t\right| \tag{S.7}$$

in (rad/s) units, using all the ^{1}H in the system and the last 6.5536 ns of the simulation.

Since we are evaluating an anisotropic effect of the system from a periodic cubic simulation box, which is inherently anisotropic due to the cubic shape[26] and absence of angular momentum conservation.[27,28] Note that it is also well known that pair correlations evince periodicity artifacts which become pronounced near the vertices and edges of the cubic simulation box.[29–31] Hence, we need to exercise caution while evaluating Eq. 7.

The following steps were taken to remove simulation artifacts. The inner sum is only evaluated for hydrogens j with $r_{ij} < 15$ Å from the hydrogen i. The RDC was also evaluated for three primary axes $\vec{x}$, $\vec{y}$, and $\vec{z}$, and the mean RDC was used for further computations. For CS1000a, we once again assume each matrix carbon atom as a site for ^{1}H dipole. The simulation box is still not expected to preserve isotropy, so we compute the RDC for bulk heptane $\Delta\omega_{RDC}^{\text{bulk}}$, which serves as a baseline given bulk heptane is isotropic. Hence, the difference between confined heptane and bulk is used to determine $T_{2,RDC}$ as such

$$\frac{1}{T_{2,RDC}} = \Delta\omega_{RDC} - \Delta\omega_{RDC}^{\text{bulk}} \tag{S.8}$$

resulting in the following values:

Table S2: List of $\Delta\omega_{RDC}$ values using Eq. S.7, along with $T_{2,RDC}$ using Eq. S.8

Confining matrix	$\Delta\omega_{RDC}$ (k-rad/s)	$\Delta\omega_{RDC} - \Delta\omega_{RDC}^{\text{bulk}}$ (k-rad/s)	$T_{2,RDC}$ (ms)
Bulk	1.55	0	∞
CS1000a	13.3	11.8	0.085
Polymer 5:95	10.3	8.70	0.120
Kerogen-IIC	13.4	11.8	0.085

S.4 Experimental details

The Kimmeridge Shale originated from the coast of Dorset in the United Kingdom, and is the same as in Refs. 32, 33, and 19. LECO and RockEval measurements found a total organic carbon of $TOC \simeq 10.1$ wt% (or $\simeq 17.6$ vol% equivalently), a hydrogen index of HI $\simeq 684$ mg_HC/g_orgC, an oxygen index of OI $\simeq 12$ mg_$CO_{(2)}$/g_orgC, and a $T_{max} \simeq 424$ °C, indicating Type II immature kerogen, or specifically Type II-A (immature) according to Ungerer *et al.* classification.[9] This is more immature than the simulated kerogen, which is Type II-C (middle-end of oil window).

The kerogen isolation procedure can be found in Ref. 19, resulting in a high organic-matter content of $TOC \simeq 68$ wt% (or $\simeq 84$ vol% equivalently). The dry kerogen powder was then pelletized in an 8 mm diameter pellet press with an (axial) pelletizing stress of 51,000 psi. An example of the pellets is shown in Fig. S10, where the total dry mass was $\simeq 1$ g. Also shown in Fig. S10 is an SEM (scanning electron microscope) image of the kerogen grains and the inter-granular pore-space. The pellets were then vacuum-saturated by applying a high vacuum for 2 hours followed by saturation with n-heptane at 5000 psia hydrostatic pressure for 4 days. Saturation with heptane resulted in $\simeq$50% swelling of the bulk volume of the pellets, where the swelling took place mostly along the axial direction, i.e., in the direction of the axial stress during pelletization.

The NMR data were acquired on an Oxford Instruments GeoSpec2 rock-core analyzer at a resonance frequency of $f_0 = 2.3$ MHz (similar to wireline NMR logging tools) using a customized 18 mm probe. The pellets were placed in a sealed glass tube, and left for one hour in the spectrometer to equilibrate to 30°C before data acquisition. The 2D T_1-T_2 data were acquired with 32 log-spaced inversion recovery steps ranging from 0.1 to 1000 ms for T_1 encoding, followed by a CPMG (Carr, Purcell, Meiboom, Gill) train with an echo spacing of $t_E = 0.1$ ms for T_2 encoding.

The 2D maps were processed using Tiknonov regularization[34,35] with 120 log-spaced bins ranging from 10^{-2} ms to 10^3 ms for both T_1 and T_2. The total porosity ϕ_T is reported in

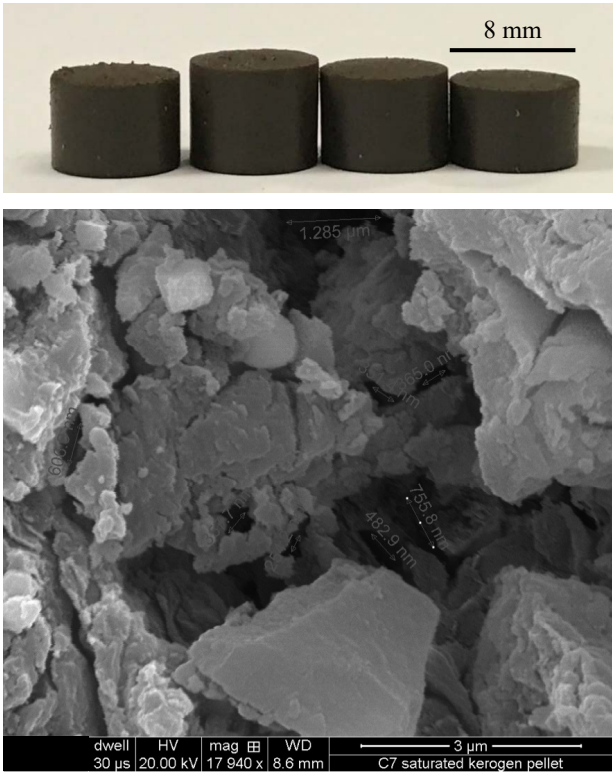


Figure S10: Picture of kerogen pellets (top) isolated from the Kimmeridge Shale. SEM (scanning electron microscope) image of the crushed pellets after heptane saturation (bottom). Images are taken from Ref. 32 and 19.

"pu", i.e. porosity units, or percent of bulk volume, equivalently, where the NMR hydrogen index of $HI = 1.0028$ for n-heptane is taken into account.

The cutoff separating the inter-granular heptane from the dissolved heptane is chosen to be $T_2 = 2$ ms (dashed vertical line). The inter-granular porosity $\phi_>$ above $T_2 > 2$ ms, the intra-granular porosity $\phi_<$ below $T_2 < 2$ ms, and the total NMR porosity $\phi_T = 44.5$ pu are related by:

$$\phi_T = \phi_< + \phi_> \quad \text{(pu)} \tag{S.9}$$

$$\phi_\mu = \frac{\phi_<}{1 - \phi_>} \quad \text{(vol\%)}, \tag{S.10}$$

and $\phi_\mu = 13.6$ vol% is the "micro-porosity", i.e. the dissolved-heptane porosity of the kerogen grain in vol%. The units of the y-axis of the 1D distributions $P(T_1)$ and $P(d)$ are

in (vol%/div), which stands for volume percent per "division". A division, defined as div $= \log_{10}(T_{1,i+1}) - \log_{10}(T_{1,i})$, is the logarithmic bin spacing, which is independent of index i. This unit convention ensures that a square distribution a decade wide and unit height has an area of 1 vol%.

Note that in addition to cross-relaxation effects in T_1 between all ^{1}H's as a result of spin diffusion,[36,37] there is also diffusive coupling (for both T_1 and T_2) between inter-granular and dissolved heptane as a result of molecular diffusion.[19] These two phenomena, i.e., spin diffusion and molecular diffusion, have distinct physical origins, though they are often confused with each other.

References

(1) Jain, S. K.; Pellenq, R. J.-M.; Pikunic, J. P.; Gubbins, K. E. Molecular Modeling of Porous Carbons Using the Hybrid Reverse Monte Carlo Method. *Langmuir* **2006**, *22*, 9942–9948.

(2) Falk, K.; Coasne, B.; Pellenq, R.; Ulm, F. J.; Bocquet, L. Subcontinuum Mass Transport of Condensed Hydrocarbons in Nanoporous Media. *Nat. Commun.* **2015**, *6*, 1–7.

(3) Shah, J. K.; Marin-Rimoldi, E.; Mullen, R. G.; Keene, B. P.; Khan, S.; Paluch, A. S.; Rai, N.; Romanielo, L. L.; Rosch, T. W.; Yoo, B.; Maginn, E. J. Cassandra: An open source Monte Carlo package for molecular simulation. *J. Comput. Chem.* **2017**, *38*, 1727–1739.

(4) Shah, J. K.; Maginn, E. J. A general and efficient Monte Carlo method for sampling intramolecular degrees of freedom of branched and cyclic molecules. *J. Chem. Phys.* **2011**, *135*, 134121.

(5) Martin, M. G.; Siepmann, J. I. Transferable potentials for phase equilibria. 1. United-atom description of n-alkanes. *J. Phys. Chem. B* **1998**, *102*, 2569–2577.

(6) Theoretical and Computational Biophysics group, NIH Center for Macromolecular Modeling and Bioinformatics, at the Beckman Institute, University of Illinois at Urbana-Champaign, NAMD. 2018; `http://www.ks.uiuc.edu/Research/namd/`.

(7) Phillips, J. C.; Braun, R.; Wang, W.; Gumbart, J.; Tajkhorshid, E.; Villa, E.; Chipot, C.; Skeel, R. D.; Kale, L.; Schulten, K. Scalable Molecular Dynamics with NAMD. *J. Comput. Chem.* **2005**, *26*, 1781–1802.

(8) ParamChem, CGenFF 3.0.1. `https://cgenff.paramchem.org`, 2020.

(9) Ungerer, P.; Collell, J.; Yiannourakou, M. Molecular Modeling of the Volumetric and

Thermodynamic Properties of Kerogen: Influence of Organic Type and Maturity. *Energy Fuels* **2015**, *29*, 91–105.

(10) Sandia National Laboratories, LAMMPS. `http://lammps.sandia.gov`, 2022.

(11) Plimpton, S. Fast parallel algorithms for short-range molecular dynamics. *J. Comput. Phys.* **1995**, *117*, 1–19.

(12) Yiannourakou, M.; Ungerer, P.; Leblanc, B.; Rozanska, X.; Saxe, P.; Vidal-Gilbert, S.; Gouth, F.; Montel, F. Molecular Simulation of Adsorption in Microporous Materials. *Oil Gas Sci. Technol.– Rev. IFP Energies nouvelles* **2013**, *68*, 977–994.

(13) Sun, H.; Mumby, S. J.; Maple, J. R.; Hagler, A. T. An Ab Initio CFF93 All-Atom Force Field for Polycarbonates. *J. Amer. Chem. Soc.* **1994**, *116*, 2978–2987.

(14) France-Lanord, A.; Rigby, D.; Mavromaras, A.; Eyert, V.; Saxe, P.; Freeman, C.; Wimmer, E. MedeA®: Atomistic simulations for designing and testing materials for micro/nano electronics systems. 2014 15th International Conference on Thermal, Mechanical and Mulit-Physics Simulation and Experiments in Microelectronics and Microsystems (EuroSimE). 2014; pp 1–8.

(15) Collell, J.; Ungerer, P.; Galliero, G.; Yiannourakou, M.; Montel, F.; Pujol, M. Molecular Simulation of Bulk Organic Matter in Type II Shales in the Middle of the Oil Formation Window. *Energy Fuels* **2014**, *28*, 7457–7466.

(16) Nosé, S. A molecular dynamics method for simulation in the canonical ensemble. *Mol. Phys.* **1984**, *52*, 255–268.

(17) Hoover, W. G. Canonical dynamics: Equilibrium phase-space distribution. *Phys. Rev. A* **1985**, *31*, 1695–1697.

(18) Hoover, W. G. Constant-Pressure Equations of Motion. *Phys. Rev. A* **1986**, *34*, 2499.

(19) Singer, P. M.; Chen, Z.; Wang, X.; Hirasaki, G. J. Diffusive Coupling in Heptane-Saturated Kerogen Isolates Evidenced by NMR T_1-T_2 and T_2-T_2 Maps. *Fuel* **2020**, *280*, 118626.

(20) Yeh, I.-C.; Hummer, G. System-Size Dependence of Diffusion Coefficients and Viscosities from Molecular Dynamics Simulations with Periodic Boundary Conditions. *J. Phys. Chem. B* **2004**, *108*, 15873–15879.

(21) Singer, P. M.; Valiya Parambathu, A.; Wang, X.; Asthagiri, D.; Chapman, W. G.; Hirasaki, G. J.; Fleury, M. Elucidating the ^{1}H NMR Relaxation Mechanism in Polydisperse Polymers and Bitumen using Measurements, MD Simulations, and Models. *J. Phys. Chem. B* **2020**, *124*, 4222–4233.

(22) Valiya Parambathu, A.; Singer, P. M.; Hirasaki, G. J.; Chapman, W. G.; Asthagiri, D. Critical Role of Confinement in the NMR Surface Relaxation and Diffusion of *n*-heptane in a Polymer Matrix Revealed by MD Simulations. *J. Phys. Chem. B* **2020**, *124*, 3801–3810.

(23) McConnell, J. *The Theory of Nuclear Magnetic Relaxation in Liquids*; Cambridge University Press, 1987.

(24) Cowan, B. *Nuclear Magnetic Resonance and Relaxation*; Cambridge University Press, 1997.

(25) Washburn, K. E.; Cheng, Y. Detection of Intermolecular Homonuclear Dipolar Coupling in Organic Rich Shale by Transverse Relaxation Exchange. *J. Magn. Reson.* **2017**, *278*, 18–24.

(26) Allen, M. P.; Tildesley, D. J. *Computer Simulation of Liquids*, 2nd ed.; Oxford University Press: Cambridge, UK, 2017.

(27) Hoover, W. G. *Molecular dynamics*; Springer-Verlag: Berlin, 1986.

(28) Kuzkin, V. On Angular Momentum Balance for Particle Systems with Periodic Boundary Conditions. *Z. Angew. Math. Mech.* **2015**, *95*, 1290–1295.

(29) Mandell, M. J. On the Properties of a Periodic Fluid. *J. Stat. Phys.* **1976**, *15*, 299–305.

(30) Pratt, L. R.; Haan, S. W. Effect of Periodic Boundary Conditions on Equilibrium Properties of Computer Simulated Fluids I. Theory. *J. Chem. Phys.* **1981**, *74*, 1864–1872.

(31) Pratt, L. R.; Haan, S. W. Effect of Periodic Boundary Conditions on Equilibrium Properties of Computer Simulated Fluids II. Application to Simple Liquids. *J. Chem. Phys.* **1981**, *74*, 1873–1876.

(32) Singer, P. M.; Chen, Z.; Hirasaki, G. J. Fluid Typing and Pore Size in Organic Shale Using 2D NMR in Saturated Kerogen Isolates. *Petrophysics* **2016**, *57*, 604–619.

(33) Chen, Z.; Singer, P. M.; Kuang, J.; Vargas, M.; Hirasaki, G. J. Effects of Bitumen Extraction on the 2D NMR Response of Saturated Kerogen Isolates. *Petrophysics* **2017**, *58*, 470–484.

(34) Venkataramanan, L.; Song, Y.-Q.; Hürlimann, M. D. Solving Fredholm Integrals of the First Kind with Tensor Product Structure in 2 and 2.5 Dimensions. *IEEE Trans. Sig. Process.* **2002**, *50*, 1017–1026.

(35) Song, Y.-Q.; Venkataramanan, L.; Hürlimann, M. D.; Flaum, M.; Frulla, P.; Straley, C. T_1-T_2 Correlation Spectra Obtained Using Fast Two-Dimensional Laplace Inversion. *J. Magn. Reson.* **2002**, *154*, 261–268.

(36) Washburn, K. E. Relaxation Mechanisms and Shales. *Concepts Magn. Reson.* **2014**, *A 43*, 57–78.

(37) Singer, P. M.; Asthagiri, D.; Chen, Z.; Valiya Parambathu, A.; Hirasaki, G. J.; Chapman, W. G. Role of Internal Motions and Molecular Geometry on the NMR Relaxation of Hydrocarbons. *J. Chem. Phys.* **2018**, *148*, 164507.